






**Melting curve of vanadium up to 256 GPa: Consistency between experiments and theory**

Youjun Zhang <sup>1</sup>, Ye Tan <sup>2</sup>, Hua Y. Geng,<sup>2</sup> Nilesh P. Salke,<sup>3</sup> Zhipeng Gao,<sup>2</sup> Jun Li <sup>2,\*</sup>, Toshimori Sekine,<sup>4</sup>  
Qingming Wang,<sup>1</sup> Eran Greenberg <sup>5,†</sup>, Vitali B. Prakapenka,<sup>5</sup> and Jung-Fu Lin <sup>6,‡</sup>

<sup>1</sup>*Institute of Atomic and Molecular Physics, Sichuan University, Chengdu 610065, China*

<sup>2</sup>*National Key Laboratory for Shock Wave and Detonation Physics, Institute of Fluid Physics, CAEP, Mianyang 621900, China*

<sup>3</sup>*Department of Physics, University of Illinois at Chicago, Chicago, Illinois 60607, USA*

<sup>4</sup>*Center for High Pressure Science and Technology Advanced Research, Shanghai 201203, China*

<sup>5</sup>*Center for Advanced Radiation Sources, University of Chicago, Chicago, Illinois 60637, USA*

<sup>6</sup>*Department of Geological Sciences, Jackson School of Geosciences, The University of Texas at Austin, Austin, Texas 78712, USA*



(Received 3 October 2020; revised 12 November 2020; accepted 16 November 2020; published 3 December 2020)

The melting curve of vanadium at high pressure and temperature (P-T) is of great interest to our understanding of *d*-orbital transition metals with simple crystal structures at extreme P-T conditions. Here we have investigated the melting curve and crystal structures of polycrystalline vanadium at high P-T using synchrotron x-ray diffraction (XRD) in laser-heated diamond anvil cells (LH DACs) up to  $\sim 100$  GPa and  $\sim 4400$  K, a two-stage light-gas gun with *in situ* shock temperature measurements up to  $\sim 256$  GPa and  $\sim 6200$  K, and *ab initio* molecular dynamics (AIMD) with density functional theory computations up to  $\sim 200$  GPa. The occurrence of the diffuse scattering signals in high P-T XRD patterns is used as the primary criterion to determine the melting curve of body-centered cubic (bcc) vanadium up to  $\sim 100$  GPa in LH DACs. Analysis of thermal radiation spectra of shocked vanadium using a quasispectral pyrometer constrains the melting curve up to  $\sim 246$  GPa and  $\sim 5830$  K, which is consistent with our static results using the Simon equation. The present static and dynamic experiments on the melting curve of vanadium are consistent with our AIMD simulations with the two-phase melting modeling, and are overall consistent with other theoretical simulations using the Z method. The results reconcile the recently reported theoretical discrepancy, and refute a higher melting curve report given by self-consistent *ab initio* lattice dynamics calculations. The consistencies among our studies indicate that one does not have to invoke superheating as a hypothesis to describe the solid-liquid equilibrium boundary of vanadium as an explanation for static vs dynamic experimental results. Our static and dynamic results with *in situ* diagnostics of melting and two-phase AIMD simulation have implications for studying melting curves of other *d*-orbital transition metals and their alloys at extreme P-T conditions.

DOI: [10.1103/PhysRevB.102.214104](https://doi.org/10.1103/PhysRevB.102.214104)

## I. INTRODUCTION

Phase diagrams and melting behaviors of *d*-orbital transition metals with simple crystal structures at high pressure and temperature (P-T) are of fundamental interest in condensed matter physics and materials science [1–8]. Among the *d*-orbital transition metals, a number of elements including vanadium (V), niobium (Nb), tantalum (Ta), chromium (Cr), molybdenum (Mo), tungsten (W), and iron (Fe) are stable in a body-centered cubic structure (bcc, space group  $Im\bar{3}m$ ), one of the simplest crystal structures, at ambient conditions. Even with the bcc crystal structure, these transition metals and their compounds can exhibit very distinct physical properties and have thus attracted particular interest in materials science applications such as new functional materials (e.g., refractory alloys [9,10]) [5,11–14]. The transition metals also occur naturally in the cores of the Earth and other planets where

iron is the most abundant element [15–20]. Therefore, there are significant interest in knowing their P-T phase diagrams and physical properties for materials and planetary science applications.

Extensive studies on the phase diagrams of the bcc transition metals including melting curves have been conducted using laser-heated static diamond anvil cells (LH DACs) and shock compression experiments as well as theoretical calculations [5,12,14,21]. However, reliable determinations of the high P-T phase diagram and melting curve, especially above 100 GPa and 4000 K, remain very challenging. Previous experiments using LH DACs and shock compressions have reported melting curves on V [14,22], Fe [23,24], Ta [12,21], and Mo [5,25,26]. While some static and dynamic results have converged with each other (Ref. [27]), discrepancies in other metals between different approaches still exist [28,29]. As an example, the melting points determined by the shock experiments and the extrapolations of static experimental results for V [14], Ta [12], Mo [5], and W [2,30] show a large discrepancy of  $\sim 3000$  K at  $\sim 300$  GPa, which is far beyond the reported experimental uncertainties. Such a large discrepancy makes it difficult to benchmark theoretical calculations and to establish physical models of simple metals at

<sup>†</sup>Present address: Applied Physics Department, Soreq Nuclear Research Center (NRC), Yavne 81800, Israel.

<sup>\*</sup>lijun102@caep.cn

<sup>‡</sup>afu@jsg.utexas.edu

extremes. So far, a number of hypotheses have been invoked to explain these inconsistencies including diagnostic techniques for detecting melting and structures, stress-strain rates, superheating effect, and mechanical responses in static vs dynamic experiments [7,31], but the consistency and reliability between experiments and theories require further confirmation using multiple reliable experimental and theoretical constraints.

Vanadium has recently attracted attention because it is one of the few transition metals with the simplest bcc structure below the melting curve [14,32–34]. Under compression in the solid, the bcc-V phase transforms to the rhombohedral phase (rh, space group  $R\bar{3}m$ ) [33] at  $\sim 30$ –69 GPa and 300 K. The transition appears to be sensitive to hydrostaticity and deviatoric stress environment in the sample chambers [32,33,35]. Recently, both first-principles calculations (Ref. [34]) and high P-T XRD experiments in LH-DACs (Ref. [14]) found that the rh-V phase transforms back to the bcc-V phase upon heating at high pressure. However, the melting curve of vanadium at high pressure remains controversial among results in DAC experiments, shock experiments, and theoretical computations. Early static DAC experiments up to  $\sim 80$  GPa reported a relatively low and nearly “flat” melting curve of vanadium using the laser-speckle method as a diagnostics [2]. Recent high P-T experiments using diffuse scattering signals of liquid vanadium in *in situ* XRD coupled with LH DACs or the plateaus feature between the temperature and laser power relationship (Ref. [14]) have indicated a melting temperature of  $\sim 3800$  K at  $\sim 80$  GPa that was  $\sim 1000$  K higher than that using the laser-speckle method (Ref. [2]). It has been argued that the reported melting curve of vanadium using the laser-speckle method was likely affected by the recrystallization of vanadium at high P-T and thus is not a good indicator of melting.

Shock experiments using sound velocity and pyrometer measurements have provided additional constraints on the melting temperature of vanadium at shock pressures of 150–250 GPa [22]. However, the reported melting point of  $\sim 7800$  K at  $\sim 230$  GPa in the shock experiment (Ref. [22]) is  $\sim 2000$ –4000 K higher than the extrapolated value in the recent DAC works (Ref. [14]). These previous shock experiments may have suffered from a large uncertainty in shock temperature determinations because the pyrometer used only had six channels with discrete wavelengths between 400 and 800 nm [22]. In recent shock temperature measurements for iron using proper shock temperature measurements and sample assemblages, the determined shock melting curve of iron is consistent with that in static LH-DAC experiments [27]. This reconciliation encourages us to reinvestigate the shock melting curve of vanadium under shock loading and compare the results with LH-DAC experiments.

Early *ab initio* lattice dynamics calculations at high P-T showed melting temperatures of vanadium that are more consistent with shock experimental results with higher melting temperatures, e.g.,  $\sim 8000$  K at  $\sim 182$  GPa [36], but recent computations using *ab initio* molecular dynamics (AIMD) and the  $Z$  method based on density-functional theory (DFT) indicate much lower melting curves that are generally consistent with the extrapolation from new LH-DAC results [14,37]. Additionally, recent theoretical predictions by the  $Z$  method

(Ref. [14]) indicate  $\sim 300$ –500 K higher melting temperatures than that of a two-phase method by AIMD simulations (Ref. [37]) up to  $\sim 250$  GPa. This difference remains to be confirmed by accurate experiments and theory at such high pressures. In AIMD simulations, the two-phase method and the *heat until it melts* (HUM) method are two typical means to obtain the melting curve of a material, where the former can usually give a more reliable result than the HUM using experimental results as a reference, but the latter can converge more rapidly [38]. The  $Z$  method was developed to combine the advantages of both methods [39], but there is still a discrepancy between the two approaches especially at ultrahigh pressure [38,40]. Therefore, further static and dynamic experiments with reliable diagnostics of melting and temperature measurements, as well as accurate theoretical calculations, are needed to better constrain the melting curve of vanadium at high P-T.

Here we report the melting curve of vanadium up to  $\sim 250$  GPa using experimental results from *in situ* XRD in LH DACs and pyrometer measurements in shock compression, together with theoretical predictions using AIMD. Diffuse scattering signals from molten vanadium in synchrotron XRD experiments are used as a major criterion to determine melting, while analysis of crystalline textures is used to provide additional constraints on the melting curve and the fast recrystallization of vanadium at high P-T [5]. In shock experiments, we measured the shock temperatures of vanadium across its solid-liquid phase boundary using a 16-channel time-resolved quasispectral pyrometer in a two-stage light-gas gun. In theoretical calculations, the two-phase method using DFT and AIMD simulations is employed to locate the melting points accurately. The melting temperature of vanadium is determined to be  $\sim 5830$  K at the pressure of  $\sim 246$  GPa. Our static and shock experimental results are consistent with each other and also with our two-phase theoretical predictions. These results are applied to understand the melting curves of other  $d$ -block transition metals at high P-T.

## II. METHODS

### A. *In situ* synchrotron x-ray diffraction measurements in LH DACs

High P-T experiments were performed using double-sided LH DACs with a pair of diamond anvils of 200  $\mu\text{m}$  or beveled diamond anvils of 150–300  $\mu\text{m}$  culets (a beveled angle of  $9^\circ$ ). Polycrystalline vanadium with  $>99.9\%$  purity purchased from Alfa Aesar was used as the starting material. The powder sample was compressed into a thin disk 6–8  $\mu\text{m}$  thick between a pair of diamond anvils with 1000- $\mu\text{m}$  culets. A piece of  $\sim 50$ –80- $\mu\text{m}$ -wide disk was then loaded into a sample chamber of  $\sim 100$   $\mu\text{m}$  diameter drilled in a rhenium gasket, which was sandwiched between two dried KCl layers with a thickness of  $\sim 5$   $\mu\text{m}$  each (Fig. S1 in the Supplemental Material [41]). KCl was dried in a vacuum oven for 8 h before loading into a DAC, and was used as the pressure-transmitting medium and pressure calibrant, as well as thermal insulator. A small piece of ruby was also loaded into the sample chamber and used as a pressure calibrant for initial pressure increase before XRD experiments.

*In situ* synchrotron XRD experiments in LH DACs were performed at the beamline 13-IDD of GSECARS at the Advanced Photon Source. An incident x-ray wavelength of  $\lambda = 0.3344 \text{ \AA}$  was focused to a spot size of  $\sim 3 \times 4 \text{ \mu m}$  [full width at half maximum (FWHM)] onto the sample, and diffracted signals were collected using a Pilatus CdTe 1M detector. The loaded samples were compressed to targeted pressures at room temperature, where the chamber pressure was determined from the equation of state of KCl using the lattice parameter measured by *in situ* XRD [42] and cross checked with the equation of state of vanadium [14,33]. Subsequently, two infrared laser beams were focused onto both sides of the sample with flat-top laser spots of  $\sim 8\text{--}10 \text{ \mu m}$  in diameter. The thermal radiation spectra of the heated samples were measured and then fitted to the Planck function with graybody approximation to determine the temperatures of the samples [43]. To avoid possible sample contaminations and diamond failures during heating [5], a burst-laser heating procedure with a heating duration of 1–2 s was used to heat the samples between 1000 and 4400 K. A Pilatus detector was synchronized with the burst heating to timely collect diffraction patterns at high P-T. Multiple temperature measurements were conducted within XRD exposure time to evaluate temperature fluctuations, which were typically  $\sim 5\%$  or less of the measured temperatures [44]. A fresh and unheated spot of the sample was selected for each new heating cycle at a given pressure point so XRD patterns were collected from pristine sample regions (Fig. S1(b) in the Supplemental Material [41]).

### B. Shock temperature measurements by optical pyrometer in a two-stage light-gas gun

High purity (>99.9%) polycrystalline vanadium in the bulk form 2–3 mm thick without any observable porosity was used as the starting material in the shock experiments. Single-crystal LiF with the [100] orientation ( $\sim 20 \text{ mm}$  in diameter and  $\sim 8 \text{ mm}$  in thickness) was used as the window attached to the vanadium sample to allow continuous optical observations of the thermal radiance at the V/LiF interface. The vanadium sample and LiF crystal were polished to a surface roughness below  $\sim 20 \text{ nm}$  and a flatness below  $\sim 100 \text{ nm}$ , and were then assembled to ensure a smooth V/LiF interface boundary (Fig. S2 in the Supplemental Material [41]). The LiF window has optical transparency without shock-induced extinction [45]. The sample box was evacuated before shots to minimize the optical background from the residual air. Pure copper (Cu) and Ta disks ( $\sim 25 \text{ mm}$  in diameter) were used as the flyers. A schematic diagram of the setup is shown in Fig. S2 in the Supplemental Material [41], while details of the shock temperature measurements can be found in previous works [27,46,47].

Hypervelocity impact experiments were conducted using a 30-mm-bore two-stage light-gas gun at the Institute of Fluid Physics, China. Impact velocities (5.78–6.77 km/s) were measured within  $\sim 1\%$  uncertainty by an optic beam breakout (OBB) method, where the time-interval counters were triggered by laser-beam interrupts. Using previous sound velocity measurements as the initial reference [22], the vanadium sample was shocked to pressures of  $\sim 210\text{--}240 \text{ GPa}$  to cross over its solid-liquid phase boundary. The impact conditions are

listed in Table I, including the measured impact velocities and the derived Hugoniot and interface pressures from the reported Hugoniot relations of vanadium [48] and LiF window [45], as well as the Cu [49,50] and Ta [51] flyers. Thermal emissions of the shocked sample were measured from the V/LiF interface using a quasispectral optical pyrometer consisting of 16 channels and 10-nm narrow bandpass filters with a high time resolution of  $\sim 3 \text{ ns}$  in the wavelength range of 400–800 nm [46,47]. The use of the quasispectral pyrometer setup improved the temperature measurement accuracy as compared with the previous shock temperature measurements in Ref. [22].

### C. Melting temperature calculations by *ab initio* molecular dynamics and DFT

First-principles calculations were carried out to determine the high-pressure melting curve of vanadium. In the calculations, we used the finite temperature DFT of Mermin, the projector augmented-wave (PAW) pseudopotential for the ion-electron interaction (where 13 electrons and the inner 3s orbital were treated in the valence space), and the generalized gradient approximation of Perdew, Burke, and Ernzerhof (PBE) for the exchange-correlation functionals in the electron subsystem, as implemented in VASP. The two-phase method (TPM), in which a solid-liquid coexistence interface is introduced into the initial configurations for the subsequent *NPT* ensemble (representing the conservation of the total number of atoms, the pressure, and the temperature) AIMD simulations, is used to locate the melting temperature at the given pressure theoretically. The two-phase method bracketed the melting point by tracing the evolution of the liquid/solid interface at a number of temperatures, which provided us an estimate for the error bars of the calculated melting points. The supercells of AIMD simulation contain up to 350 atoms with periodic boundary conditions. A  $2 \times 2 \times 2$  Monkhorst-Pack grid was utilized for the *k*-point sampling to guarantee the high precision of the simulations, with the electronic temperature set to the equilibrium ionic temperature, which is controlled by a Nosé-Hoover thermostat. The energy cutoff for the plane-wave basis set of the wave functions is 300 eV.

The AIMD simulation time was set for 3 ps with a time step of 0.5 fs. Since the melting or solidification process of a metal usually takes less than 2 ps to complete, results from the last 1 ps of the calculations are used to evaluate the statistics of some specific properties such as energy and density. The initial interphase configuration in the two-phase simulations was prepared by heating the system up to a sufficiently high temperature to be fully melted, with half of the atoms fixed. This treatment created a physical interface between the two phases (liquid/solid) without an artificial gap so each of the two subsystems was fully equilibrated before they were thermodynamically combined. The convergence quality of the electronic self-consistent field, the conditions of thermodynamic equilibration, and ergodicity in AIMD were also checked. We employed three different thermostats including the Nosé-Hoover thermostat, Andersen thermostat, and Langevin thermostat in the simulations to approach the ergodicity as closely as possible. The last two thermostats are stochastic and beneficial to remove dynamical corrections

TABLE I. Hugoniot and partially released states of vanadium in the pyrometer experiments under shock loading.  $V_{\text{imp}}$  is the measured impact velocity of the flyer,  $u_{pi}$  is the particle velocity of the LiF/V interface, and  $P_l$  is the partially released (interface) pressure.  $u_p$  and  $U_s$  are the particle velocity and shock velocity of vanadium sample, respectively, at the shock Hugoniot pressure of vanadium ( $P_H$ ). The Hugoniot parameters used in this study are  $U_s = 5.044 + 1.242u_p$  (km/s) with the density of  $6.087 \text{ g/cm}^3$  for vanadium [48],  $U_s = 3.310(0.008) + 1.296(0.005)u_p$  (km/s) with the density of  $16.684(0.03) \text{ g/cm}^3$  for Ta [51],  $U_s = 3.933(0.004) + 1.500(0.025)u_p$  (km/s) with the density of  $8.939(5) \text{ g/cm}^3$  for Cu [49,50], and  $U_s = 5.215(0.02) + 1.351(0.03)u_p$  (km/s) with the density of  $2.640(0.002) \text{ g/cm}^3$  for LiF [45]. The uncertainties including measurement and propagation errors are given in parentheses at  $2\sigma$  levels.

Shot No.	Flyer	Window	$V_{\text{imp}}$ (km/s)	$u_{pi}$ (km/s)	$P_l$ (GPa)	Hugoniot state of vanadium		
						$u_p$ (km/s)	$U_s$ (km/s)	$P_H$ (GPa)
T1	Ta	LiF	5.78(6)	4.609(40)	139.2(2.1)	3.663(37)	9.59(0.06)	213.9(3.2)
T2	Cu	LiF	6.77(7)	4.755(48)	146.2(2.3)	3.784(39)	9.74(0.07)	224.5(3.5)
T3	Ta	LiF	6.36(6)	5.051(46)	160.5(2.3)	4.026(40)	10.04(0.07)	246.1(3.4)
T4	Ta	LiF	6.52(7)	5.173(53)	166.7(2.7)	4.129(44)	10.17(0.07)	255.7(3.9)

among particles. The coincidence of the results from these thermostats implies our simulations in this system are close to being ergodic. The reported values in this study are simulated using the Langevin thermostat. With this approach here, the theoretical melting curve of vanadium is accurately determined with a temperature uncertainty of about 100 K up to 200 GPa. Further details of the simulation methods can also be found elsewhere [52,53].

### III. RESULTS AND DISCUSSION

#### A. Bcc-rh phase boundary of vanadium at high P-T by *in situ* x-ray diffraction

The bcc-structured vanadium is expected to be the primary phase before melting at high pressure, but its solid phase transition needs to be confirmed to ensure that the melting behavior is probed properly. Diffraction patterns of solid vanadium at high P-T were thus collected using synchrotron *in situ* XRD with  $\sim 2 \mu\text{m}$  in the spatial resolution and 1–2 s in the collection time. The phase structure of vanadium was determined from room temperature up to  $\sim 4400$  K in the pressure range of 20–100 GPa (Fig. 1). At room temperature and pressures below  $\sim 44$  GPa, XRD patterns were identified as bcc V [Fig. 1(a)]. With increasing pressure above  $\sim 52$  GPa, the split of the (110) bcc-V peak into (1-10) and (100) rh-V peaks, as well as the (211) bcc-V peak into (2-1-1), (2-10), and (110) rh-V peaks, are clearly observed in the diffraction patterns [Fig. 1(a)] [32,33]. The fitted lattice parameters of rh V at  $\sim 52$  GPa and room temperature are  $a_R = 2.4459(5) \text{ \AA}$  and  $\alpha = 109.9(2)^\circ$ . The pressure of the bcc-rh phase transition is consistent with the previous observations at  $\sim 53$  GPa using NaCl as the pressure medium [14]. Our experimental results show that rh V is stable at pressures of 50–100 GPa and room temperature. At 52 GPa, the rh-V phase is stable with increasing temperature by laser heating from  $\sim 300$  to 1407 K, but it transformed back to bcc with increasing temperatures from  $\sim 300$  to  $\sim 1881$  K, where the lattice parameter,  $a_b$ , in bcc V was  $2.8212(9) \text{ \AA}$  [Fig. 1(b)]. Previous phonon dispersion measurements and computations also show that the pressure-induced bcc-rh phase transition in vanadium is due to the softening of the transverse acoustic phonon near the Brillouin zone center along its  $[\xi, 0, 0]$  direction [54,55].

The stability of rh V is proposed to be reduced by its high electron temperatures due to the thermoelectron effect [34].

We analyzed the FWHM of the (110) bcc-V peak at high P-T from the collected XRD patterns. The FWHM increases from  $0.10^\circ$  at  $\sim 33$  GPa to  $0.18^\circ$  at  $\sim 52$  GPa due to the split and broadening of the (110) bcc-V peak into (1-10) and (100) rh-V peaks [Fig. 2(b)], while with increasing temperature from  $\sim 300$  to  $\sim 1600$  K, the FWHM of the combined (1-10) and (100) rh-V diffraction peaks continuously decreased from  $\sim 0.18^\circ$  to  $0.10^\circ$  (e.g., 52, 66, and 90 GPa, Fig. 2). Consequently, rh V transformed back to the bcc-V phase at temperatures above  $\sim 1600$  K. The bcc V underwent fast recrystallization with strong spotty diffraction patterns at tem-

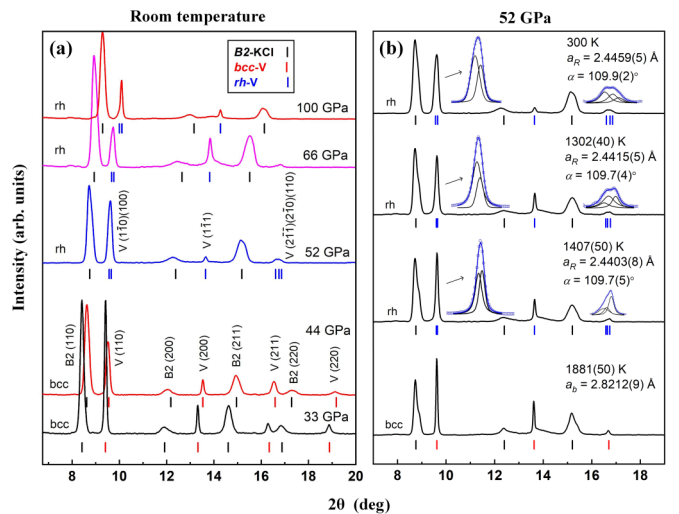


FIG. 1. Representative x-ray diffraction patterns of vanadium at high P-T. (a) Bcc-V phase transforms to the rh-V phase at pressures above  $\sim 52$  GPa. Vertical red, blue, and black lines are the Bragg diffraction positions of bcc V, rh V, and B2 KCl, respectively. (b) The rh-V phase transforms to the bcc V phase with increasing temperature at  $\sim 52$  GPa. The pressure of  $\sim 52$  GPa was determined at ambient temperature ( $\sim 300$  K). LeBail refinements of x-ray diffraction patterns for the rh V phase are also plotted in (b) as insets (open blue circles with blue lines) to highlight the peak broadening feature. The wavelength of the incident x-ray source was  $0.3344 \text{ \AA}$ . KCl in the B2 phase was used as the thermal insulator and pressure calibrant.



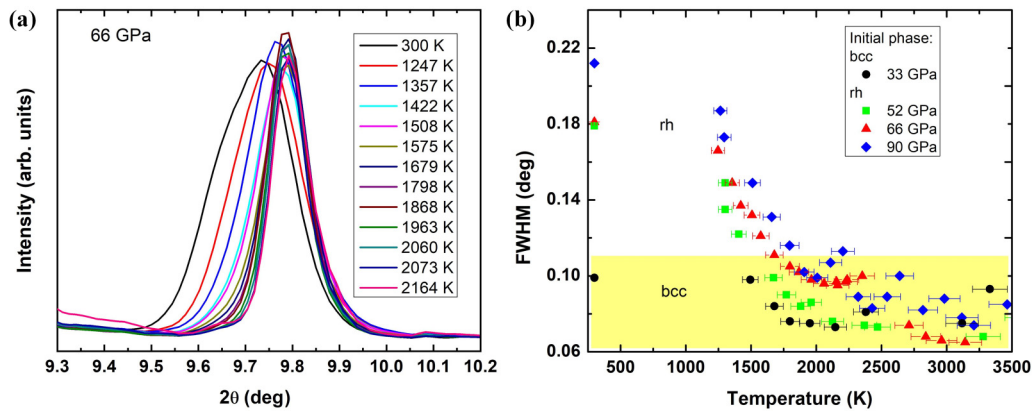


FIG. 2. Full width at half maximum (FWHM) of the diffraction peaks of vanadium at high P-T. (a) Evolution of the combined (1-10) and (100) diffraction peaks in rh V with increasing temperatures at  $\sim 66$  GPa. The exposure time for each spectrum was 2 s. The temperature uncertainty in (a) is typically within  $\sim 5\%$  of the reported temperature. (b) FWHMs of (110) peak in bcc V and (1-10) and (100) peaks in rh V as a function of temperature at four selected pressures. The yellow region represents much narrower FWHMs below  $\sim 0.12^\circ$ , which is identified as the occurrence of the bcc V phase at elevated temperatures at each given pressure.

peratures of above  $\sim 2000$ – $2100$  K and pressures of  $\sim 52$  and  $\sim 77$  GPa (Figs. 3(b) and S3 [41]). Consistent with the literature nomenclature such as polycrystalline iron at high P-T [24], we referred to this temperature range as “fast recrystallization threshold ( $T_R$ )” upon heating. The FWHM of the (110) bcc-V peak decreases to  $0.6^\circ$ – $0.8^\circ$  across the “fast recrystallization” line [Fig. 2(b)].

### B. Melting of vanadium by x-ray diffraction in LH DACs

*In situ* XRD measurements in LH DACs are also used to determine the melting curve of bcc-structured vanadium at high pressure. At each given pressure, we incrementally increased the laser power to achieve the required high temperatures in DACs. X-ray diffraction images were recorded during and after each step of burst laser heating to characterize the crystalline textures of vanadium at high P-T. The textures of vanadium changes in increments due to the short heating duration of each burst (1–2 s), which allowed us to trace the evolution of its texture with temperature [5,24]. The present *in situ* XRD spectra indicate that bcc V remains stable at high temperatures before melting at pressures up to  $\sim 100$  GPa [Fig. 3(a)]. The occurrence of the diffuse scattering signals in liquid vanadium provides an unambiguous signature of the melting of bcc-structured vanadium. For example, the diffuse signals of vanadium appeared above the melting temperature ( $T_M$ ) of  $\sim 3857$  K at  $\sim 52$  GPa and  $\sim 4192$  K at  $\sim 77$  GPa [Fig. 3(a)]. The reported high P-T data for the melting curve of vanadium in Fig. 4 have taken its thermal pressure during laser heating into account. Considering that the thermal insulator KCl in the sample chamber has a very low thermal expansivity (a low  $\alpha K_T$  parameter of  $\sim 0.0022$  GPa/K for B2 KCl) [42], the thermal pressure of the heated vanadium ( $P_{\text{thermal}}$ ) can be estimated to be approximately half of the maximum thermal pressure ( $\alpha K_T \Delta T$ ) for vanadium under constant volume condition, where  $\alpha$  is the thermal expansion coefficient [ $4.6(6) \times 10^{-5} \text{ K}^{-1}$ ] and  $K_T$  is the isothermal bulk modulus [152(4) GPa]. The literature thermal equation of state data of vanadium are used for the estimates (Ref. [14]). The estimated thermal pressures at high P-T along the melting

curve of vanadium are typically on the order of a few GPa increase (Fig. 4).

The texture changes of vanadium with temperature at high pressures are used as additional information to constrain the melting temperature. The textures of the vanadium samples were analyzed during and after laser heating at high P-T [Figs. 3(b) and 3(c)]. The XRD images of vanadium at different temperature ranges show three distinct textural features. When polycrystalline bcc V was heated to temperatures below  $T_R$ , its fine-grained features remained [e.g., at  $\sim 2007$  K and  $\sim 77$  GPa, Figs. 3(b) and 3(c)]. At heating temperatures between  $T_R$  and  $T_M$ , the XRD images displayed spotty patterns as shown in Fig. 3(b), indicating the growth of texture with preferentially oriented grains in bcc V due to the fast recrystallization during heating. In addition, the textured vanadium is temperature quenchable as Fig. 3(c) shows. When the sample was heated to above melting  $T_M$  (e.g., at  $\sim 4192$  K and  $\sim 77$  GPa), the diffraction peaks of bcc V disappeared and the diffuse scattering rings of liquid vanadium appeared [Fig. 3(b)]. After temperature quenching from above  $T_M$ , the fine-grained and continuous Debye rings in the XRD images were observed [Fig. 3(c)], indicating randomly oriented grains in quenched vanadium. The diffuse scattering signals of the liquid during heating and the fine-grained texture of the temperature-quenched vanadium melt are both used to define the melting curve of vanadium. Our observed textural features of the heated vanadium are consistent with the changes of the crystalline microstructures in Mo at high P-T by LH DACs [5]. The melting points of vanadium at pressures of 20–100 GPa were determined using the aforementioned melting criteria in LH DACs (open red circles, Fig. 4).

Using all of the XRD results together, we have constructed the high P-T phase diagram of vanadium up to  $\sim 100$  GPa and  $\sim 4400$  K including the rh-bcc phase boundary, fast recrystallization threshold, and melting curve (Fig. 4). The transition temperature between rh and bcc V is  $\sim 1500$ – $1600$  K and nearly flat at pressures of 52–100 GPa, which is generally consistent with the previous first-principles calculations (Ref. [34]). Compared with literature XRD experimental results in LH DACs [14], the phase boundary between rh and

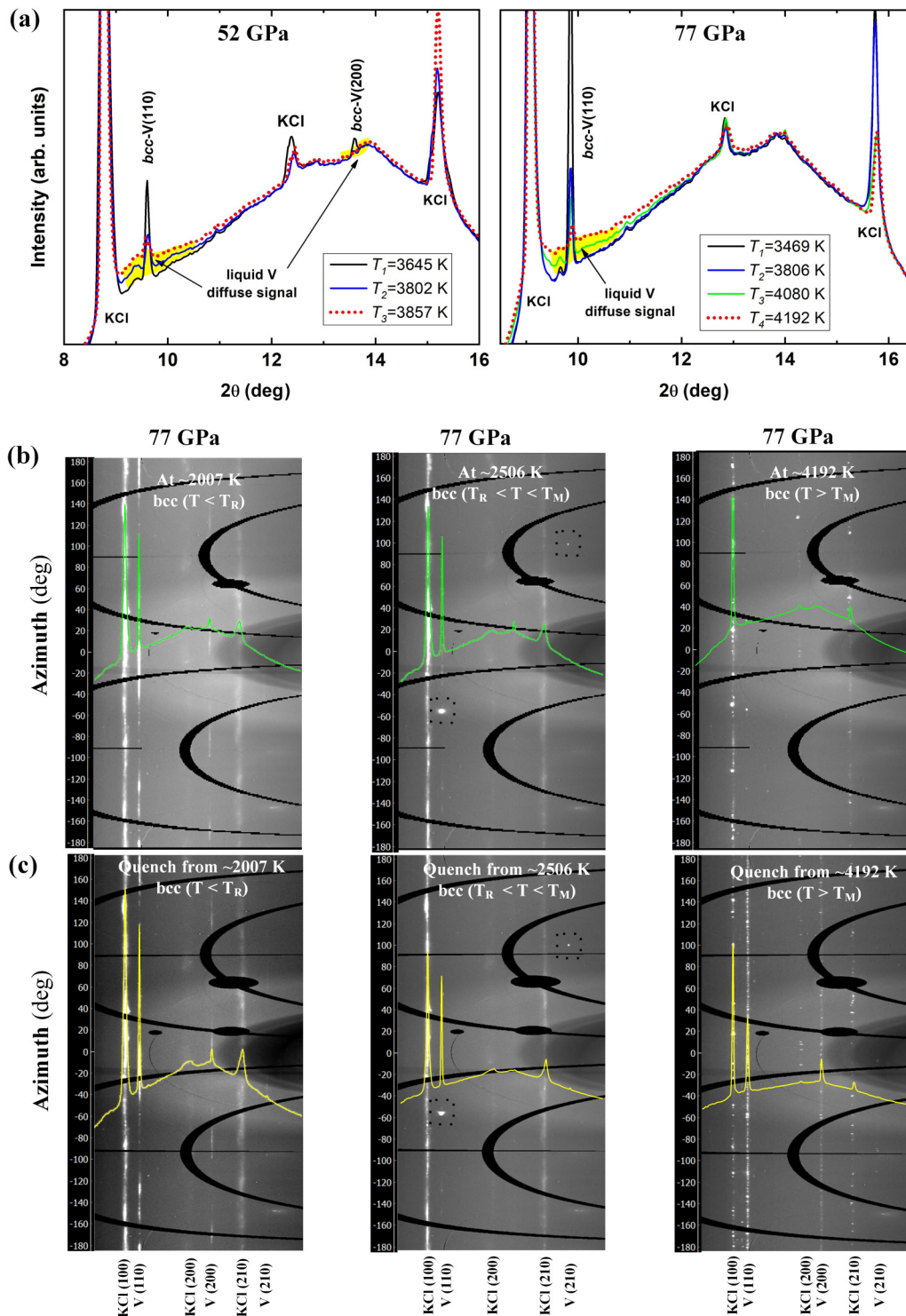


FIG. 3. X-ray diffraction patterns of vanadium during and after laser heating at high pressure. (a) Integrated diffraction patterns of vanadium during heating at 52.0(0.5) and 77(1) GPa. The observation of diffuse scattering rings (yellow regions) is indicative of the occurrence of liquid vanadium. Azimuthally unwrapped x-ray diffraction images of vanadium during laser heating (b) and after temperature quenching (c) at  $\sim 77(1)$  GPa. The patterns taken from  $\sim 2007$  K in (b) and after quenching in (c) show continuous diffraction rings of polycrystalline vanadium. The patterns taken from  $\sim 2506$  K in (b) and after quenching in (c) show large spotty patterns of crystalline vanadium (in the boxes), indicating grain growth textures due to fast recrystallization. The pattern taken from  $\sim 4192$  K in (b) shows diffuse scattering signals of the liquid, and the pattern after quenching from  $\sim 4192$  K in (c) displays continuous rings, which are indicative of fine-grained polycrystalline vanadium from the fast temperature-quenched liquid. The integrated x-ray diffraction patterns shown as green lines in (b) and yellow lines in (c) are also plotted for comparisons.

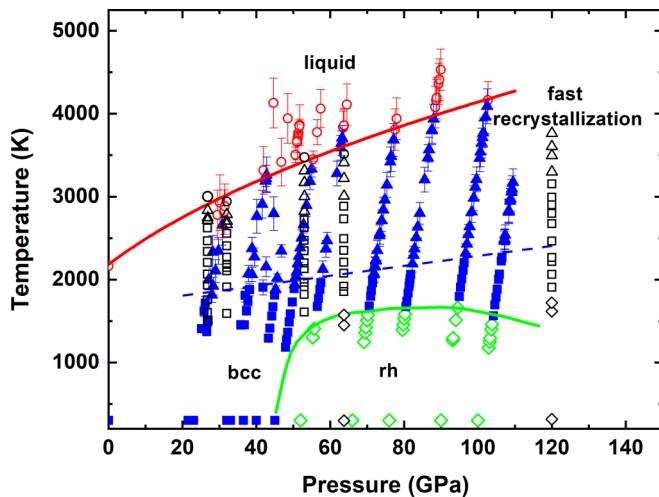


FIG. 4. Phase diagram of vanadium at high P-T determined by *in situ* x-ray diffraction in LH DACs. The experimentally observed phases are displayed as solid blue squares (polycrystalline bcc), open green diamonds (polycrystalline rh), solid blue triangles (bcc fast recrystallization), and open red circles (liquid). The solid green line represents the bcc-rh phase boundary. The dashed blue line represents the fast recrystallization threshold of bcc V at high temperatures. The solid red curve represents the modeled melting curve of the measured melting points using the Simon law. Literature x-ray diffraction results [14] are also plotted for comparisons, where open black squares, diamonds, triangles, and circles represent the polycrystalline bcc, polycrystalline rh, fast recrystallization in bcc, and liquid vanadium, respectively.

bcc V agrees well with each other. The fast recrystallization threshold of bcc V at high P-T in the present study is signifi-

cantly lower than the results in Ref. [14]. The difference here is likely a result of different heating durations (continuous vs burst laser heating) and/or initial sample thickness ( $\sim 5$  vs  $6-8 \mu\text{m}$ ) in these studies, although original XRD images reporting the large spots of recrystallized vanadium were not available for direct comparisons (Figs. 3(b) and 3(c) and S3 [41]).

### C. Shock temperatures and melting of vanadium under shock compression

The interface temperatures between vanadium and the LiF window under shock compression were measured using a two-stage light-gas gun to determine the melting temperatures of vanadium along the Hugoniot. Shock pressures were determined using the impedance matching method from the measured impact velocity and known Hugoniot equations of state for Ta [51] and Cu [49,50] flyers, LiF window [45], and vanadium sample [48]. Four shots were performed at the shock pressures of 214–256 GPa (Table I), which were designed to target the shock melting curve of vanadium based on the previous measurements of the longitudinal sound velocity [22]. The corresponding V/LiF interface pressures are from  $\sim 139$  to 167 GPa. Typical high time-resolution radiant spectra of shocked vanadium at the interface are shown in Fig. 5(a), which were obtained from a 16-core silica fiber probe in the pyrometer. The collected emission intensity remains steady in the time interval between points A and B, which corresponds to the arrival times of the shock and rarefaction waves at the V/LiF interface, respectively [Fig. 5(a)]. The interface temperature ( $T_i$ ) and emissivity ( $\epsilon$ ) were determined by fitting the emission spectra intensity to Planck's equation for a graybody

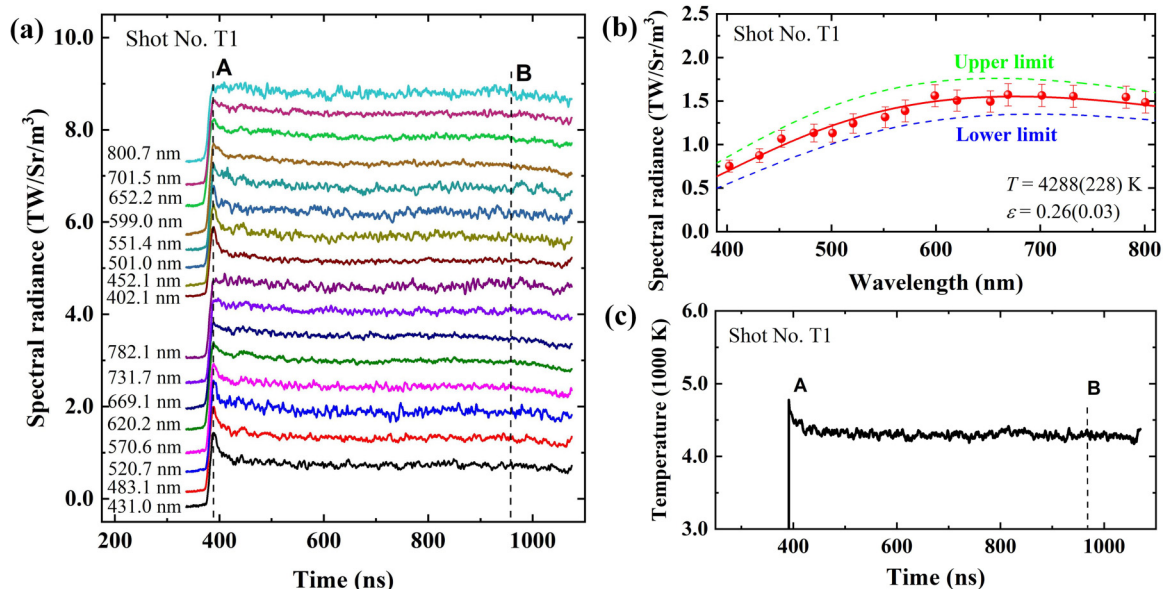


FIG. 5. Temperature measurements of shocked vanadium using thermal radiation spectral radiance. (a) Typical spectral radiance profiles measured in vanadium by a 16-channel quasispectral pyrometer at the V/LiF interface pressure of 139.2(2.1) GPa (shot no. T1). Fitting the measured spectral radiance using Planck's radiation equation yields an emissivity ( $\epsilon$ ) of 0.26(0.03) and a temperature of 4288(228) K (b). The determined temperature profile during shock compression is shown in (c). Blue and green dashed lines represent the lower and upper limits of the measured temperature, respectively. Points A and B indicate the arrivals of the shock and rarefaction waves at the V/LiF interface, respectively.



TABLE II. Hugoniot and melting temperatures of vanadium under shock compression.  $T_I$  is the measured temperature at the V/LiF interface pressure  $P_I$  by the pyrometer experiments.  $T_w$  and  $\kappa_w$  are the shock temperature and thermal conductivity of LiF window at  $P_I$  [68], respectively. The thermal conductivity of vanadium ( $\kappa_s$ ) at high P-T is still unclear, so we used the thermal conductivity of  $\sim 35$  W/m/K at ambient conditions [69]. It is noted that high P-T can modify the thermal conductivity of transition metals, e.g., in iron [70,71]. If the thermal conductivity of vanadium at high P-T differs by a factor of 2–3 with the value at ambient conditions, it will introduce an extra uncertainty of  $\sim 100$  K for the Hugoniot temperatures.

Shot No.	$T_I$ at $P_I$ (K)	$T_w$ at $P_I$ (K)	$\kappa_w$ at $P_I$ (W/m/K)	$\alpha$	$T_R$ (K)	$T_H$ at $P_H$ (K)	$T_m$ at $P_I$ (K)
T1	4288(228)	3250(300)	3.1(0.4)	2.5	4696(272)	5426(338)	4492(291)
T2	4330(287)	3370(400)	3.0(0.4)	2.6	4700(323)	5433(380)	4515(347)
T3	4617(272)	3430(400)	2.6(0.4)	2.8	5041(310)	5834(369)	4829(344)
T4	4900(293)	3470(400)	2.4(0.4)	2.9	5390(329)	6242(385)	—

radiation function [Fig. 5(b)]. The fitting function is defined as follows [46]:

$$N_{\text{expt}}(\lambda, \varepsilon, T_I) = \varepsilon C_1 \lambda^{-5} [\exp(C_2/\lambda T_I) - 1]^{-1}, \quad (1)$$

where  $N_{\text{expt}}$  is the spectral radiance, the radiation constants are  $C_1 = 1.19106 \times 10^{-16}$  W m<sup>2</sup>/Sr and  $C_2 = 1.43878 \times 10^{-2}$  m K, and the emissivity is assumed to be independent of wavelength. A typical fitting of the spectral radiance vs wavelength at the interface pressure of  $\sim 139.2$  GPa is shown in Fig. 5(b), and the results for the other three shots are shown in Fig. S4 in the Supplemental Material [41]. Analysis of the thermal radiation spectra with a time resolution of 3 ns provided the time-resolved temperature profile during the shock compression [Fig. 5(c)]. The time-dependent temperature profile remains nearly constant during shock compression except in the first  $\sim 20$  ns of the shock-wave arrival [time point A, Fig. 5(c)], where a spike peak of  $\sim 400$  K appeared due to the shock-induced flash from the interfacial residual gas.

The shock temperature  $T_H$  of vanadium was then determined from the measured  $T_I$  through a Mie-Grüneisen thermal relation [23,56]:

$$T_H = T_R \exp \left[ - \int_{V_R}^{V_H} (\gamma/V) dV \right], \quad (2)$$

$$T_R = T_I + \frac{(T_I - T_W)}{\alpha}, \quad (3)$$

$$\alpha = \left[ \frac{(\rho C \kappa)_S}{(\rho C \kappa)_W} \right]^{1/2}, \quad (4)$$

where  $T_W$  is the LiF window temperature, and  $\rho$ ,  $C$ , and  $\kappa$  are the density, heat capacity, and thermal conductivity, respectively, at the interface pressure  $P_I$  for the vanadium sample (subscript: S) and window (subscript: W) (Table II). The measured shock temperatures of vanadium are shown in Fig. 6(b) (red circles). Based on the previous sound velocity data [Fig. 6(a)], our results indicate that vanadium starts to melt along the Hugoniot at 213.9(3.2) GPa and 5426(338) K, and melting completes at 246.1(3.4) GPa and 5834(369) K. The present shock temperatures of vanadium are  $\sim 1000$ –2000 K lower than the previous results at 200–250 GPa by Ref. [22] [Fig. 6(b)]. We observed a discontinuity in the present Hugoniot temperature which is taken as the melting point from

solid Hugoniot to liquid Hugoniot, but this behavior was not found in Ref. [22] [Fig. 6(b)]. The pyrometer used in Ref. [22] had only six channels in the wavelength range, which was not sufficient to reliably derive an accurate temperature from

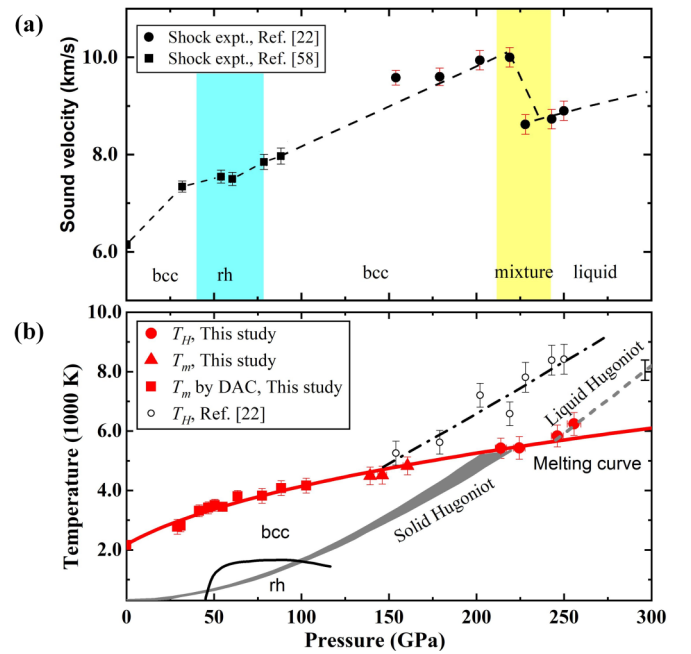


FIG. 6. Melting temperature of vanadium determined from longitudinal sound velocity and shock temperature measurements at high pressure. (a) A sharp decrease of the longitudinal sound velocity at  $\sim 210$ –240 GPa (solid black circles) is indicative of shock-induced vanadium melting [22]. The drop in the longitudinal sound velocity of vanadium at  $\sim 40$ –80 GPa is due to the bcc-rh phase transition under shock loading (solid black squares) [58]. The dashed lines are plotted to guide the eyes for the sound velocity evolution during shock. (b) High P-T phase diagram and Hugoniot states of vanadium. Shock temperatures along the Hugoniot states ( $T_H$ , solid red circles) and melting temperatures at partially released (interface) states ( $T_m$ , solid red triangles) are plotted using results from this study. Previously reported shock Hugoniot temperatures of vanadium in Ref. [22] are also plotted for comparisons (open black circles and dash-dot line). The gray band represents the calculated solid Hugoniot temperatures of vanadium, where the lower and upper boundaries are from Refs. [14] and [37], respectively. The dashed gray line represents the liquid Hugoniot temperatures of vanadium.



the graybody fit to the measured thermal radiation spectra; additionally, their sample was sputtered onto a sapphire window  $\sim 4 \mu\text{m}$  thick [22], which might have introduced porosity and/or an imperfect sample/window interface.

Our experimental results on the melting temperature are generally consistent with the recently calculated solid Hugoniot  $T_H$  of vanadium by *ab initio* molecular dynamics and DFT with the Z method [gray band in Fig. 6(b)]. Liquid Hugoniot  $T_H$  of vanadium is then obtained using the measured shock temperatures above  $\sim 246$  GPa [gray dashed line, Fig. 6(b)], whereas solid Hugoniot  $T_H$  is reduced by  $\Delta T \approx 1200(200)$  K across melting due to the latent heat of melting for vanadium. The entropy change ( $\Delta S$ ) across melting can thus be estimated to be  $\sim 0.66R$  ( $R$ : gas constant) by the equation of  $\Delta S = C_V(\Delta T/T_{om})$ , where  $C_V$  is the heat capacity of vanadium ( $\approx 0.49 \text{ J/g K} \approx 3R$ ), and  $T_{om}$  is the melting temperature of  $\sim 5426$  K at the onset melting pressure of  $\sim 214$  GPa. The estimated  $\Delta S$  is consistent with the approximated value of melting for simple substances ( $\approx R \ln 2$ ) [57]. If we use the calculated Hugoniot temperature and our determined phase diagram of vanadium, we can also constrain the bcc-rh phase boundary on the Hugoniot. Figure 6(b) indicates that the solid Hugoniot P-T of vanadium crosses the rh phase boundary at  $\sim 46$  GPa and  $\sim 600$  K and at  $\sim 95$  GPa and  $\sim 1600$  K, respectively. The longitudinal sound velocity data of shocked vanadium also show a softening across the same pressure range [Fig. 6(a)] [22,58]. The sound velocity recovers normal behavior upon further shock pressure increase because the rh V transforms back to the bcc phase at the Hugoniot pressure of above  $\sim 90$  GPa.

When a metal or an alloy is shocked to the pressure on the solid-liquid boundary, its partial release path follows the melting boundary through an isentropic release and subsequently thermal conduction at the sample/window interface [27,59]. Therefore, the melting temperature ( $T_m$ ) of vanadium at the V/LiF interface pressure ( $P_I$ ) can also be obtained from the measured  $T_I$  through a one-dimensional heat conduction model [21]:

$$T_m \cong T_I + (T_I - T_W)/(2\alpha) = (T_I + T_R)/2. \quad (5)$$

We obtained the melting temperatures of vanadium at the interfacial pressures of 139–167 GPa [solid triangles, Fig. 6(b)], which partially released from the Hugoniot pressures of 214–246 GPa (Table I). As a result, the melting temperatures of vanadium are determined at pressures from  $\sim 139$  to 246 GPa in this study. The present shock experimental results are consistent with the extrapolation of our static LH-DACs results [Fig. 6(b)]. Using the melting points derived from our static and shock experimental results, the melting curve of vanadium can be modeled using the Simon-Glatzel equation:

$$T_m = T_0 \left( \frac{P - P_0}{a} + 1 \right)^{\frac{1}{b}}, \quad (6)$$

where the parameters are  $a = 26.3(3.9)$ ,  $b = 2.45(0.16)$ , and  $T_0 = 2183$  K at ambient pressure  $P_0$ . The melting curve of vanadium has an initial Clapeyron slope ( $dT_m/dP$ ) of 33.9 K/GPa at ambient pressure, which is overall consistent with the previous values of 31.4–32.6 K/GPa [14,60]. The melting slope gradually decreases with pressure to 13.4 K/GPa at 100 GPa and 7.6 K/GPa at 300 GPa.

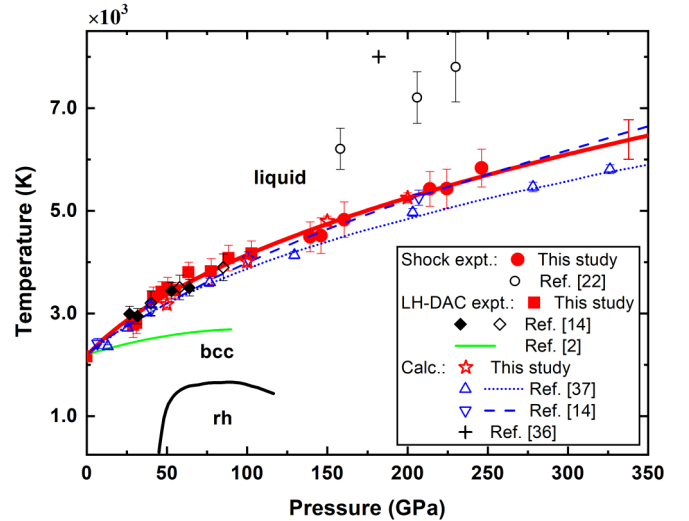


FIG. 7. High P-T phase diagram and melting curve of vanadium at high pressure. The red line is the Simon-Glatzel fit to the present melting points from *in situ* XRD experiments in LH DACs (solid red squares) and shock pyrometer experiments (solid red circles). The open star squares are our calculated melting temperatures of vanadium by *ab initio* molecular dynamics based on DFT and the two-phase method. The solid and open black diamonds are the melting points determined from XRD and temperature vs laser power plateau in LH DACs in Ref. [14], respectively. The open black circles are the melting points from shock experiments in Ref. [22]. The solid green line is the melting curve determined by the laser-speckle method in LH-DACs [2]. The open blue triangles and inverted triangles are the calculated melting temperatures of vanadium by *ab initio* molecular dynamics (Ref. [37]) and DFT Z-method techniques (Ref. [14]), respectively, where the blue short-dashed and dashed curves are used to show their trends, respectively. The symbol “+” represents the estimated upper bound of the melting temperature of vanadium by phonon dispersion calculations at high P-T [36].

#### D. Melting curves of vanadium and other *d*-orbital transition metals

Figure 7 compares the melting curve of vanadium from this study with literature data from previous experiments and theoretical calculations. At pressures below 100 GPa, the present melting curve of vanadium determined by *in situ* XRD experiments is  $\sim 1000$  K higher than previous ones using the laser-speckle method in LH DACs in Ref. [2] (green line, Fig. 7). Fast recrystallization and melting are endothermic, and the speckles observed in Ref. [2] were likely affected by the recrystallization that is indistinguishable optically at high temperatures. Considering the error bars in the high P-T melting curve of vanadium, the melting curve in our study is overall consistent with literature results determined by *in situ* XRD (solid black diamonds, Fig. 7) and temperature vs laser-power plateaus (open black diamonds, Fig. 7) in a continuously LH DAC (Ref. [14]).

The present melting curve of vanadium at shock pressures above 100 GPa is  $\sim 1000$ – $2000$  K lower than that in previous shock experiments in Ref. [22] (open black circles, Fig. 7). The consistency in the melting results of bcc V between the present shock and static experiments indicate a minor effect of strain rate on the melting temperature of the simple structured

metal. This result is also supported by our calculated melting curve using AIMD-DFT and the two-phase method (open squares in Fig. 7), as well as by the Z method calculation implemented with quantum molecular dynamics of DFT (open inverted triangles, Fig. 7) [14]. In particular, our calculation employed the standard two-phase method for melting modeling. The melting curves of vanadium by these two methods are very consistent with each other. However, the theoretical results reported in Ref. [37] by AIMD technique are systematically  $\sim 10\%$  lower (open triangles, Fig. 7), especially at high pressures above 200 GPa. This small discrepancy (about 310 K at  $\sim 200$  GPa) can originate in the low calculation precision as employed in Ref. [37]. The measured melting points of vanadium in this study are closer to our standard two-phase method and the calculations using the Z method (Fig. 7), indicating that our work successfully reconciles the previously reported theoretical data in Refs. [14,37]. The fact that the Z method can describe the melting behavior of vanadium well indicates that superheating of solid vanadium does not occur in dynamic experiments. On the other hand, previous phonon dispersion calculations of vanadium at high P-T using the self-consistent *ab initio* lattice dynamics method (Ref. [36]) suggested a significantly higher melting point than our experimental results (plus symbol, Fig. 7) and theoretical predictions. The discrepancy could be explained by an overestimation of the stability of rh V at high temperatures in previous theoretical calculations [34].

Our work shows the convergence of the melting curve of vanadium among results from static and dynamic experiments as well as theoretical calculations. The consistency here indicates that the melting curves of other *d*-block transition metals at high P-T can also be reliably determined using the protocol established here. On the other hand, the inconsistencies in the previously reported melting curves between static and shock experiments such as Mo [5], Ta [61], and W [2,30] at pressures of 200–300 GPa can be interpreted as a result of different melting diagnostics used, which varies by 2000–3000 K and thus needs to be reinvestigated. We, therefore, have plotted the melting curves of representative *d*-orbital transition metals for comparisons, including 3*d* transition metals of V (this study), Fe (Refs. [24,27]), and Ni (Ref. [62]); 4*d* of Zr (Ref. [63]) and Mo (Ref. [5]); and 5*d* of Ta (Ref. [12]) and Pt (Ref. [64]) (Fig. 8). These elements are selected as their melting curves were determined using similar melting diagnoses in LH DACs and/or shock compression. Specifically, the melting curves of V and Fe taken from both shock and static experiments are consistent with each other, while the melting curves of other metals are taken from LH-DAC experiments with *in situ* XRD diagnosis (Table S1 in the Supplemental Material [41]). These results show that the 5*d* transition metals (Pt and Ta) have higher melting temperatures than other 3*d* and 4*d* metals at high pressures. Interestingly, Pt (5*d*) has a relatively lower melting temperature at ambient pressure than some 4*d* (Mo) or 5*d* (Ta) transition metals, but its melting slope ( $dT_m/dP$ ) is much steeper than the others. Except for Pt, the melting slopes of these typical *d*-orbital transition metals flatten significantly with increasing pressure. The relatively flat melting curve at ultrahigh pressure indicates that the volume change ( $\Delta V$ ) of melting for most *d*-orbital transition metals becomes smaller with increasing pressure than the entropy change ( $\Delta S$ ) accord-

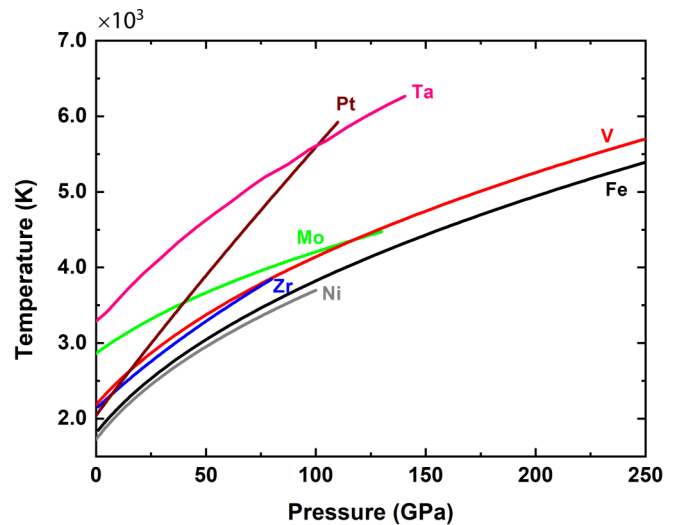


FIG. 8. Melting curves of representative transition metals V, Mo, Ta, Zr, Fe, Ni, and Pt at high pressures. The melting curves of these transition metals are determined by *in situ* XRD in LH DACs and/or quasispectral pyrometer measurements in shock compression. The melting curves of V (this study) and Fe (Refs. [24,27]) up to  $\sim 250$  GPa are obtained from *in situ* XRD and shock pyrometer experiments, which are consistent with each other. The melting curves of Ni (Ref. [62]), Zr (Ref. [63]), Mo (Ref. [5]), Ta (Ref. [12]), and Pt (Ref. [64]) are determined using *in situ* XRD in LH DACs.

ing to the Clausius-Clapeyron relation ( $\partial T_m/\partial P = \Delta V/\Delta S$ ). On the other hand, in these transition metals, V, Ta, and Mo melt from the bcc phase; Fe ( $< \sim 100$  GPa), Ni, and Pt melt from the fcc phase; and Fe ( $> \sim 100$  GPa) and Zr melt from the hcp phase. We should note that the solid structural transitions in some metals are known to affect the curvatures of their melting curves (Fig. 8). For example, it has been argued that the melting from the bcc phase should have a lower melting slope than those from fcc and hcp phases because bcc metals have a smaller packing ratio ( $\sim 0.68$ ) than fcc and hcp transition metals ( $\sim 0.74$ ), so the volume change upon melting for bcc metals can be smaller [2]. However, this reasoning does not work well according to recent works. Bcc Mo indeed has a significantly lower melting slope than Ni (fcc), Fe (fcc/hcp), and Zr (hcp), but the melting slopes of bcc V and bcc Ta do not follow this trend. Physically, the melting point of a metal depends on the (shear) strength of the metallic bond, which is sensitive to the numbers of shared delocalized electrons per atom, the size of the cation, and the compressibility, to name a few [65–67]. Further experimental and theoretical studies on the melting slopes for other *d*-orbital transition metals under high pressure are required to systematically understand their melting mechanisms.

#### IV. CONCLUSION

We have studied the melting behavior of vanadium at high pressure and temperature using complementary synchrotron x-ray diffraction in LH DACs, pyrometer measurements in a two-stage light-gas gun, and AIMD-DFT simulations with two-phase melting modeling. The appearance of diffuse scattering signals is used to determine the melting of vanadium

using synchrotron XRD in LH DACs and the changes of crystalline textures provide additional constraints on the melting behavior and the fast recrystallization of vanadium. The melting curve of vanadium has been determined up to  $\sim 100$  GPa and  $\sim 4400$  K in LH DACs. At higher pressures of 140–260 GPa, the melting temperatures of vanadium were determined using the time-resolved quasispectral pyrometer under shock loading. The derived melting temperature is  $\sim 1000$ – $2000$  K lower than previous shock data. The present shock melting curve is consistent with the extrapolated melting curve by our x-ray diffraction experiments in LH DACs. Our study reconciles the discrepancy of vanadium on the phase diagram and melting curve at high pressure and temperature under static and dynamic compressions, as well as with the theoretical predictions. The melting curve of vanadium in the present study agrees well with the recent theoretical calculations by AIMD and DFT calculations, and dismisses the theoretical discrepancy reported in Refs. [14,37]. Our results indicate that both the Z method and the AIMD-DFT simulations with the two-phase method can describe the melting behavior of vanadium at high pressure very well, which further supports the argument that there cannot be significant superheating effects in static or dynamic experiments, in sharp contrast to the previous hypothesis. This study provides us a sound methodology of combined static and dynamic

experiments and theoretical approaches to determine the phase diagrams and melting curves of *d*-orbital transition metals and their compounds at ultrahigh P-T.

#### ACKNOWLEDGMENTS

We thank J.C. Liu and J. Yang for their assistance with the synchrotron XRD experiments. We acknowledge support from the Science Challenge Project (TZ2016001), the NSF under Grant No. U1730248, the National Natural Science Foundation of China (Grants No. 11602251, No. 11672274, and No. 42074098), and the National Key Laboratory of Shock Wave and Detonation Physics (JCKYS2018212002, 6142A03182006). J.-F.L. acknowledges support from the Geophysics Program of the National Science Foundation, U.S. (Grant No. EAR-1916941). High pressure and temperature XRD experiments were conducted at GeoSoilEnviroCARS of APS, ANL. GeoSoilEnviroCARS operations are supported by the National Science Foundation–Earth Sciences (EAR-1634415) and the Department of Energy, Geosciences (Grant. No. DE-FG02-94ER14466). Part of this research used resources of the Advanced Photon Source, a U.S. Department of Energy (DOE) Office of Science User Facility operated for the DOE Office of Science by Argonne National Laboratory under Contract No. DE AC02-06CH11357.

- 
- [1] A. Landa, P. Söderlind, A. V. Ruban, O. E. Peil, and L. Vitos, *Phys. Rev. Lett.* **103**, 235501 (2009).
- [2] D. Errandonea, B. Schwager, R. Ditz, C. Gessmann, R. Boehler, and M. Ross, *Phys. Rev. B* **63**, 132104 (2001).
- [3] G. Grimvall, B. Magyar-Köpe, V. Ozoliņš, and K. A. Persson, *Rev. Mod. Phys.* **84**, 945 (2012).
- [4] R. Briggs, M. G. Gorman, A. L. Coleman, R. S. McWilliams, E. E. McBride, D. McGonegle, J. S. Wark, L. Peacock, S. Rothman, S. G. Macleod, C. A. Bolme, A. E. Gleason, G. W. Collins, J. H. Eggert, D. E. Fratanduono, R. F. Smith, E. Galtier, E. Granados, H. J. Lee, B. Nagler *et al.*, *Phys. Rev. Lett.* **118**, 025501 (2017).
- [5] R. Hrubciak, Y. Meng, and G. Shen, *Nat. Commun.* **8**, 14562 (2017).
- [6] R. Briggs, F. Coppari, M. G. Gorman, R. F. Smith, S. J. Tracy, A. L. Coleman, A. Fernandez-Pañella, M. Millot, J. H. Eggert, and D. E. Fratanduono, *Phys. Rev. Lett.* **123**, 045701 (2019).
- [7] S. M. Sharma, S. J. Turneaure, J. M. Winey, and Y. M. Gupta, *Phys. Rev. Lett.* **124**, 235701 (2020).
- [8] S. M. Sharma, S. J. Turneaure, J. M. Winey, Y. Li, P. Rigg, A. Schuman, N. Sinclair, Y. Toyoda, X. Wang, N. Weir, J. Zhang, and Y. M. Gupta, *Phys. Rev. Lett.* **123**, 045702 (2019).
- [9] P. Singh, A. Sharma, A. V. Smirnov, M. S. Diallo, P. K. Ray, G. Balasubramanian, and D. D. Johnson, *npj Comput. Mater.* **4**, 16 (2018).
- [10] G. Liu, G. J. Zhang, F. Jiang, X. Ding, Y. Sun, J. Sun, and E. Ma, *Nat. Mater.* **12**, 344 (2013).
- [11] M. C. Akin, J. H. Nguyen, M. A. Beckwith, R. Chau, W. P. Ambrose, O. V. Fat'yanov, P. D. Asimow, and N. C. Holmes, *J. Appl. Phys.* **125**, 145903 (2019).
- [12] A. Dewaele, M. Mezouar, N. Guignot, and P. Loubeyre, *Phys. Rev. Lett.* **104**, 255701 (2010).
- [13] Y. Zhang, C. Yang, A. Alatas, A. H. Said, N. P. Salke, J. Hong, and J.-F. Lin, *Phys. Rev. B* **100**, 075145 (2019).
- [14] D. Errandonea, S. G. MacLeod, L. Burakovsky, D. Santamaria-Perez, J. E. Proctor, H. Cynn, and M. Mezouar, *Phys. Rev. B* **100**, 094111 (2019).
- [15] G. Morard, S. Boccato, A. D. Rosa, S. Anzellini, F. Miozzi, L. Henry, G. Garbarino, M. Mezouar, M. Harmand, F. Guyot, E. Boulard, I. Kantor, T. Irifune, and R. Torchio, *Geophys. Res. Lett.* **45**, 11 (2018).
- [16] Y. Li, L. Vočadlo, and J. P. Brodholt, *Earth Planet. Sci. Lett.* **493**, 118 (2018).
- [17] J.-F. Lin, W. Sturhahn, J. Zhao, G. Shen, H.-k. Mao, and R. J. Hemley, *Science* **308**, 1892 (2005).
- [18] S. Tateno, K. Hirose, Y. Ohishi, and Y. Tatsumi, *Science* **330**, 359 (2010).
- [19] W. F. McDonough, *Science* **331**, 1397 (2011).
- [20] C. Münker, R. O. C. Fonseca, and T. Schulz, *Nat. Geosci.* **10**, 822 (2017).
- [21] C. Dai, J. Hu, and H. Tan, *J. Appl. Phys.* **106**, 043519 (2009).
- [22] C. Dai, X. Jin, X. Zhou, J. Liu, and J. Hu, *J. Phys. D: Appl. Phys.* **34**, 3064 (2001).
- [23] C. S. Yoo, N. C. Holmes, M. Ross, D. J. Webb, and C. Pike, *Phys. Rev. Lett.* **70**, 3931 (1993).
- [24] S. Anzellini, A. Dewaele, M. Mezouar, P. Loubeyre, and G. Morard, *Science* **340**, 464 (2013).
- [25] J. H. Nguyen, M. C. Akin, R. Chau, D. E. Fratanduono, W. P. Ambrose, O. V. Fat'yanov, P. D. Asimow, and N. C. Holmes, *Phys. Rev. B* **89**, 174109 (2014).



- [26] J. Wang, F. Coppari, R. F. Smith, J. H. Eggert, A. E. Lazicki, D. E. Fratanduono, J. R. Rygg, T. R. Boehly, G. W. Collins, and T. S. Duffy, *Phys. Rev. B* **92**, 174114 (2015).
- [27] J. Li, Q. Wu, J. Li, T. Xue, Y. Tan, X. Zhou, Y. Zhang, Z. Xiong, Z. Gao, and T. Sekine, *Geophys. Res. Lett.* **47**, e2020GL087758 (2020).
- [28] T. D. Cuong and A. D. Phan, *Vacuum* **179**, 109444 (2020).
- [29] J. Byggmästar, K. Nordlund, and F. Djurabekova, *Phys. Rev. Materials* **4**, 093802 (2020).
- [30] R. S. Hixson and J. N. Fritz, *J. Appl. Phys.* **71**, 1721 (1992).
- [31] S.-N. Luo and T. J. Ahrens, *Phys. Earth Planet. Inter.* **143–144**, 369 (2004).
- [32] Z. Jenei, H. P. Liermann, H. Cynn, J.-H. Klepeis, B. J. Baer, and W. J. Evans, *Phys. Rev. B* **83**, 054101 (2011).
- [33] Y. Ding, R. Ahuja, J. Shu, P. Chow, W. Luo, and H.-k. Mao, *Phys. Rev. Lett.* **98**, 085502 (2007).
- [34] Y. X. Wang, Q. Wu, X. R. Chen, and H. Y. Geng, *Sci. Rep.* **6**, 32419 (2016).
- [35] L. Xiong and J. Liu, *Chin. Phys. B* **27**, 036101 (2018).
- [36] A. Landa, P. Söderlind, and L. H. Yang, *Phys. Rev. B* **89**, 020101(R) (2014).
- [37] T. Zhang, S. Wang, H. Song, S. Duan, and H. Liu, *J. Appl. Phys.* **126**, 205901 (2019).
- [38] J. Bouchet, F. Bottin, G. Jomard, and G. Zérah, *Phys. Rev. B* **80**, 094102 (2009).
- [39] A. B. Belonoshko, N. V. Skorodumova, A. Rosengren, and B. Johansson, *Phys. Rev. B* **73**, 012201 (2006).
- [40] A. B. Belonoshko, L. Burakovsky, S. P. Chen, B. Johansson, A. S. Mikhaylushkin, D. L. Preston, S. I. Simak, and D. C. Swift, *Phys. Rev. Lett.* **100**, 135701 (2008).
- [41] See Supplemental Material at <http://link.aps.org/supplemental/10.1103/PhysRevB.102.214104> for experimental setups in DAC and shock experiments, x-ray diffraction images, and spectral radiance in vanadium at high pressure and temperature.
- [42] A. Dewaele, A. B. Belonoshko, G. Garbarino, F. Occelli, P. Bouvier, M. Hanfland, and M. Mezouar, *Phys. Rev. B* **85**, 214105 (2012).
- [43] G. Shen, M. L. Rivers, Y. Wang, and S. R. Sutton, *Rev. Sci. Instrum.* **72**, 1273 (2001).
- [44] V. Prakapenka, A. Kubo, A. Kuznetsov, A. Laskin, O. Shkurikhin, P. Dera, M. Rivers, and S. Sutton, *High Press. Res.* **28**, 225 (2008).
- [45] Q. Liu, X. Zhou, X. Zeng, and S. N. Luo, *J. Appl. Phys.* **117**, 045901 (2015).
- [46] Y. Zhang, T. Sekine, J.-F. Lin, H. He, F. Liu, M. Zhang, T. Sato, W. Zhu, and Y. Yu, *J. Geophys. Res.: Solid Earth* **123**, 1314 (2018).
- [47] X. Zhou, W. J. Nellis, J. Li, J. Li, W. Zhao, X. Liu, X. Cao, Q. Liu, T. Xue, and Q. Wu, *J. Appl. Phys.* **118**, 055903 (2015).
- [48] G. R. Gathers, *J. Appl. Phys.* **59**, 3291 (1986).
- [49] A. C. Mitchell and W. J. Nellis, *J. Appl. Phys.* **52**, 3363 (1981).
- [50] R. G. Kraus, J. P. Davis, C. T. Seagle, D. E. Fratanduono, D. C. Swift, J. L. Brown, and J. H. Eggert, *Phys. Rev. B* **93**, 134105 (2016).
- [51] F. Xi, K. Jin, L. Cai, H. Geng, Y. Tan, and J. Li, *J. Appl. Phys.* **117**, 185901 (2015).
- [52] H. Y. Geng and Q. Wu, *Sci. Rep.* **6**, 36745 (2016).
- [53] H. Y. Geng, Q. Wu, M. Marqués, and G. J. Ackland, *Phys. Rev. B* **100**, 134109 (2019).
- [54] D. Antonangeli, D. L. Farber, A. Bosak, C. M. Aracne, D. G. Ruddle, and M. Krisch, *Sci. Rep.* **6**, 31887 (2016).
- [55] W. Luo, R. Ahuja, Y. Ding, and H.-k. Mao, *Proc. Natl. Acad. Sci. USA* **104**, 16428 (2007).
- [56] R. Grover and P. A. Urtiew, *J. Appl. Phys.* **45**, 146 (1974).
- [57] J. L. Tallon, *Phys. Lett. A* **76**, 139 (1980).
- [58] Y. Yu, Y. Tan, C. Dai, X. Li, Y. Li, Q. Wu, and H. Tan, *Appl. Phys. Lett.* **105**, 201910 (2014).
- [59] B. M. L. Lone, G. D. Stevens, W. D. Turley, D. B. Holtkamp, A. J. Iverson, R. S. Hixson, and L. R. Veaser, *J. Appl. Phys.* **114**, 063506 (2013).
- [60] G. R. Gathers, J. W. Shaner, R. S. Hixson, and D. A. Young, *High Temp. - High Pressures* **11**, 653 (1979).
- [61] A. Karandikar and R. Boehler, *Phys. Rev. B* **93**, 054107 (2016).
- [62] O. T. Lord, I. G. Wood, D. P. Dobson, L. Vočadlo, W. Wang, A. R. Thomson, E. T. Wann, G. Morard, M. Mezouar, and M. J. Walter, *Earth Planet. Sci. Lett.* **408**, 226 (2014).
- [63] P. Parisiades, F. Cova, and G. Garbarino, *Phys. Rev. B* **100**, 054102 (2019).
- [64] S. Anzellini, V. Monteseuro, E. Bandiello, A. Dewaele, L. Burakovsky, and D. Errandonea, *Sci. Rep.* **9**, 13034 (2019).
- [65] D. D. Klug, *Physics* **3**, 52 (2010).
- [66] A. Samanta, M. E. Tuckerman, T.-Q. Yu, and Weinan E., *Science* **346**, 729 (2014).
- [67] M. Ross, R. Boehler, and D. Errandonea, *Phys. Rev. B* **76**, 184117 (2007).
- [68] P. C. Myint, E. L. Shi, S. Hamel, H. Cynn, Z. Jenei, M. J. Lipp, W. J. Evans, and M. C. Akin, *J. Chem. Phys.* **150**, 074506 (2019).
- [69] W. D. Jung, F. A. Schmidt, and G. C. Danielson, *Phys. Rev. B* **15**, 659 (1977).
- [70] J. Xu, P. Zhang, K. Haule, J. Minar, S. Wimmer, H. Ebert, and R. E. Cohen, *Phys. Rev. Lett.* **121**, 096601 (2018).
- [71] Y. Zhang, M. Hou, G. Liu, C. Zhang, V. B. Prakapenka, E. Greenberg, Y. Fei, R. E. Cohen, and J.-F. Lin, *Phys. Rev. Lett.* **125**, 078501 (2020).